

# Quantum Rationale-Aware Graph Contrastive Learning for Jet Discrimination

Md Abrar Jahin, Md. Akmol Masud, M. F. Mridha, *Senior Member, IEEE*, and Nilanjan Dey, *Senior Member, IEEE*

**Abstract**—In high-energy physics, particle jet tagging plays a pivotal role in distinguishing quark from gluon jets using data from collider experiments. While graph-based deep learning methods have advanced this task beyond traditional feature-engineered approaches, the complex data structure and limited labeled samples present ongoing challenges. However, existing contrastive learning (CL) frameworks struggle to leverage rationale-aware augmentations effectively, often lacking supervision signals that guide the extraction of salient features and facing computational efficiency issues such as high parameter counts. In this study, we demonstrate that integrating a quantum rationale generator (QRG) within our proposed Quantum Rationale-aware Graph Contrastive Learning (QRGCL) framework significantly enhances jet discrimination performance, reducing reliance on labeled data and capturing discriminative features. Evaluated on the quark-gluon jet dataset, QRGCL achieves an AUC score of 77.53% while maintaining a compact architecture of only 45 QRG parameters, outperforming classical, quantum, and hybrid GCL and GNN benchmarks. These results highlight QRGCL’s potential to advance jet tagging and other complex classification tasks in high-energy physics, where computational efficiency and feature extraction limitations persist.

**Index Terms**—quantum machine learning, graph neural network, contrastive learning, high-energy physics, jet classification

## I. INTRODUCTION

**P**ARTICLE jet tagging, a fundamental task in high-energy physics, aims to identify the originating parton-level particles by analyzing collision byproducts at the Large Hadron Collider (LHC). While traditional approaches have relied on manually engineered features, modern deep learning methods offer promising alternatives for processing vast amounts of collision data [1]. The representation of jets as collections of constituent particles has emerged as a more natural and flexible approach compared to image-based methods, allowing for the incorporation of arbitrary particle features [2]. However, the challenge of limited labeled data in particle physics necessitates innovative solutions beyond purely supervised learning approaches. Self-supervised pretraining followed by supervised fine-tuning has shown particular promise in this domain. Self-supervised contrastive learning (CL) [3] has gained

significant attention in the field of graph neural networks (GNNs) [4], leading to the development of graph CL (GCL). This approach involves pre-training a GNN on large datasets without manually curated annotations, facilitating effective fine-tuning for subsequent tasks [5].

A review of existing GCL approaches reveals a common framework that combines two primary modules: (1) graph augmentation, which generates diverse views of anchor graphs through techniques like node dropping, edge perturbation, and attribute masking, and (2) CL, which maximizes agreement between augmented views of the same anchor while minimizing agreement between different anchors. However, these methods face inherent challenges due to the complexity of graph structures, where random augmentations may obscure critical features, potentially misleading the CL process. In response to these challenges, recent studies have shifted focus towards understanding the invariance properties of GCL. The necessity for augmentations was emphasized to maintain semantic integrity, arguing that high-performing GCL frameworks should enhance instance discrimination without compromising the intrinsic semantics of the anchor graphs. Building on this foundation, invariant rationale discovery (IRD) techniques [3] were proposed, aligning closely with the objectives of GCL. These techniques highlight the importance of identifying critical features that inform predictions effectively.

Despite these advancements, gaps remain in effectively leveraging rationales for augmentation. Existing frameworks often lack supervision signals, hindering their ability to reveal and utilize the most salient features effectively. As the amount of available data increases and the computational cost of deep learning networks rises, significant computing resources will be required to execute these algorithms efficiently. To handle computational complexity, we see a move from classical networks that process bits to quantum networks that use qubits. Quantum networks leverage unique properties such as superposition and entanglement, allowing them to represent  $2^n$  characteristics from  $n$  two-dimensional complex vectors. In contrast to classical networks, which scale linearly in expressiveness, quantum networks show exponential growth as the sample size  $n$  increases [6, 7]. Recognizing the pivotal role of the rationale generator in the GCL framework, we propose enhancing this component with a quantum-based subroutine to evaluate its potential for performance improvement. Our proposed Quantum Rationale-aware Graph Contrastive Learning (QRGCL) addresses these limitations by integrating a quantum rationale generator (QRG) that autonomously identifies and reveals salient features within the graphs, ensuring that the

M. A. Jahin is with Okinawa Institute of Science and Technology Graduate University, Okinawa 904-0412, Japan (e-mail: abrar.jahin.2652@gmail.com).

M. A. Masud is with the Institute of Information Technology, Jahangirnagar University, Dhaka, 1342, Bangladesh (e-mail: akmolmasud5@gmail.com).

M. F. Mridha is with the Department of Computer Science, American International University-Bangladesh, Dhaka 1229, Bangladesh (e-mail: froz.mridha@aib.edu).

N. Dey is with the Department of Computer Science & Engineering, Techno International New Town, New Town, Kolkata, 700156, India (e-mail: nilanjan.dey@tint.edu.in).

generated augmentations retain their discriminative power. Our approach incorporates the state-of-the-art ParticleNet [2] GNN encoder network followed by a projection head, culminating in a multi-layer perceptron (MLP) classifier. Experimental results on the quark-gluon jet tagging dataset showcase the superiority of our approach, proving its capacity to capture distinguishing semantic nodes and significantly outperforming current state-of-the-art GCL and GNN methods (classical, quantum, and hybrid).

The paper is structured as follows: Section II reviews related work, while Section III describes our dataset, the proposed QRGCL model, and the benchmark models. Section IV discusses the experimental setup, and Section V presents the results and discussion. Finally, Section VI summarizes the key findings and suggests directions for future research.

## II. BACKGROUND

### A. Contrastive Representation Learning

Contrastive representation learning [8]–[11] is an effective framework for extracting meaningful representations from high-dimensional data by mapping it into a lower-dimensional space. CL uses a self-supervised approach to differentiate between positive pairs (similar data) and negative pairs (dissimilar data), particularly when labeled data is scarce. The framework consists of three components:

- 1) **Data Augmentation Module:** This module generates multiple invariant views of a given sample using invariance-preserving transformations. The goal is to create variations of the same input that retain essential characteristics, forming positive pairs, while views from different samples are negative pairs. For instance, augmenting a quark jet should retain its distinguishing features even when transformations like noise addition or spatial shifts are applied. This ensures that the learned representations remain general and robust to different data variations.
- 2) **Encoder Network:** The augmented views are processed through an encoder, which maps each view into a lower-dimensional embedding space. Each view in a pair is passed independently through the encoder, generating embeddings that capture the intrinsic features of the input data while abstracting away specific details.
- 3) **Projection Network:** While optional, the projection network is often used to adjust the dimensionality of the embeddings, enabling fine-tuning of the representation space. Typically, this is implemented as a single linear layer that transforms the encoded embeddings into a space suitable for CL objectives.

The goal is to train the encoder to minimize the distance between positive pair embeddings and maximize the distance between negative pair embeddings, enhancing representation quality for downstream tasks like classification.

### B. Quantum Contrastive Learning (QCL)

Recent studies have begun to explore how quantum computing can enhance traditional CL frameworks. Quantum systems

can potentially offer superior computational capabilities, allowing for more complex feature extraction and representation learning. One study [12] proposed a hybrid quantum-classical model for self-supervised learning, showing that small-scale QNNs could effectively enhance visual representation learning. By training quantum and classical networks together to align augmented image views, they achieved higher test accuracy in image classification than a classical model alone, even with limited quantum sampling. Another approach [9] integrates Supervised CL (SCL) with Variational Quantum Circuits (VQC) and incorporates Principal Component Analysis (PCA) for effective dimensionality reduction. This method addresses the limitations posed by scarce training data and showcases potential in medical image analysis. Experimental results reveal that this model achieves impressive accuracy across various medical imaging datasets, particularly with a minimal number of qubits (2 qubits), underscoring the benefits of quantum computing. A different research effort presents Q-SupCon [10], a fully quantum-enhanced Supervised CL (SCL) model tailored to tackle issues related to data scarcity. Experiments demonstrate that this model yields significant accuracy in image classification tasks, even with very limited labeled datasets. Its robust performance on actual quantum devices illustrates its adaptability in scenarios with constrained data availability. Furthermore, a quantum-enhanced self-supervised CL framework has been proposed for effective mental health monitoring [11]. This framework leverages a quantum-enhanced Long Short-Term Memory (LSTM) encoder to enhance representation learning for time series data through CL. The results indicate that this model significantly outperforms traditional self-supervised learning approaches, achieving high F1 scores across multiple datasets. To take advantage of QCL, as evident in these studies, we attempted to replace the classical rationale generator with a VQC in our proposed framework.

### C. Rationale-Aware Graph Contrastive Learning (RGCL) Concept

RGCL [3] represents a self-supervised CL approach that overcomes several limitations common to traditional graph CL (GCL) frameworks. Standard GCL methods often suffer from challenges such as augmentation strategies that can inadvertently alter or remove critical graph structure and semantics, and attempts to preserve graph-specific domain knowledge sometimes result in overfitting, limiting the model’s adaptability to diverse, unseen data. RGCL addresses these issues by focusing on the concept of *rationale learning*, where the essential, discriminative information for graph classification is typically concentrated within a subset of nodes or edges in the graph. In RGCL, this discriminative subset, or *rationale*, is identified and emphasized during training, allowing the model to prioritize meaningful patterns while minimizing reliance on irrelevant features. In RGCL, specialized neural networks, known as the *rationale generator (RG)*, are used to assign importance scores to each node. This generator evaluates each node’s contribution to the graph’s overall representation. The higher-score nodes form the rationale subset,

while the remaining nodes comprise the *complement* subset. The rationale subset undergoes targeted augmentations during training, capturing the core discriminative features essential for downstream tasks. In contrast, the complement subset is augmented to encourage the exploration of less critical correlations, thus avoiding overfitting and improving generalization. RGCL pipeline leverages these dual views—*rationale* and *complement*—to guide the encoder network in learning a balanced feature space. By focusing on rationale views, the model learns robust, task-relevant features, while the complement views prevent it from becoming overly sensitive to spurious relationships, fostering a more generalized understanding.

### III. METHODOLOGY

#### A. Dataset and Preprocessing

1) *High-Energy Physics Dataset*: This study uses the *Pythia8 Quark and Gluon Jets for Energy Flow* [13] dataset, a well-established dataset in high-energy physics. The dataset comprises two million simulated particle jets, evenly divided between one million quark-originated jets and one million gluon-originated jets. These jets are generated through collision events at the Large Hadron Collider (LHC) with a center-of-mass energy  $\sqrt{s} = 14$  TeV. Jets were selected based on their transverse momentum range  $p_T^{\text{jet}}$  between 500 and 550 GeV and their pseudorapidity  $|\eta^{\text{jet}}| < 1.7$ . Each jet  $\alpha$  is labeled as a quark jet ( $y_\alpha = 1$ ) or a gluon jet ( $y_\alpha = 0$ ), providing a binary classification target for model training. The kinematic distributions of the jets, along with the particle count in each jet, are visualized in Figure 2, highlighting the differences between the quark and gluon jet populations. Each particle  $i$  within a jet is characterized by several key attributes: transverse momentum  $p_{T,\alpha}^{(i)}$ , rapidity  $\eta_\alpha^{(i)}$ , azimuthal angle  $\psi_\alpha^{(i)}$ , and its Particle Data Group (PDG) identifier  $I_\alpha^{(i)}$ .

2) *Graph Representation of Jets*: A graph  $G$  is defined as a set of nodes  $V$  and edges  $E$ , represented as  $G = \{V, E\}$ . Each node  $v^{(i)} \in V$  is connected to its neighboring nodes  $v^{(j)}$  through edges  $e^{(ij)} \in E$ . In the context of this study, each jet  $\alpha$  is modeled as a graph  $J_\alpha$ , where the nodes  $v_\alpha^{(i)}$  represent the particles in the jet, and the edges  $e_\alpha^{(ij)}$  represent the interactions between these particles. Each node  $v_\alpha^{(i)}$  is associated with a set of features  $h_\alpha^{(i)}$ , which describe its properties, while the edges have attributes  $a_\alpha^{(ij)}$  that characterize the relationship between connected nodes.

The number of nodes in each graph can vary significantly, reflecting the varying number of particles within each jet. This variability is particularly pronounced in particle physics, where jets can differ greatly in their particle multiplicity. Consequently, each jet graph  $J_\alpha$  is composed of  $m_\alpha$  particles, each with  $l$  distinct features that capture various physical properties. This graph representation provides a natural way to encode the complex interactions within jets, enabling models to leverage the relational structure among particles. An illustration of this graph-based data representation, along with an example jet depicted in the  $(\psi, y)$  plane, is shown in Figure 3a. Here, particles are visualized as nodes and their interactions as edges, offering a clear view of the underlying structure and relationships within the jet.

3) *Feature Engineering*: Additional kinematic variables are derived from the original features  $(p_{T,\alpha}^{(i)}, y_\alpha^{(i)}, \psi_\alpha^{(i)})$  using the ‘Particle’ package to enhance the model’s ability to learn from the data. These engineered features include transverse mass, energy, and Cartesian momentum components, providing a more complete description of each particle’s dynamics. Specifically, the transverse mass per multiplicity  $(m_{\alpha,T}^{(i)})$  of particle  $i$  in jet  $\alpha$  is calculated as:

$$m_{\alpha,T}^{(i)} = \sqrt{m_\alpha^{(i)2} + p_{\alpha,T}^{(i)2}} \quad (1)$$

where  $m$  is the rest mass of the particle and  $p_T^{(i)}$  is its transverse momentum. Energy per multiplicity  $(E_\alpha^{(i)})$  of particle  $i$  is computed using:

$$E_\alpha^{(i)} = m_{\alpha,T}^{(i)} \cosh y_\alpha^{(i)} \quad (2)$$

Kinematic momenta components per multiplicity  $(\vec{p}_\alpha^{(i)} = (p_{x,\alpha}^{(i)}, p_{y,\alpha}^{(i)}, p_{z,\alpha}^{(i)}))$  are derived from:

$$p_{x,\alpha}^{(i)} = p_{T,\alpha}^{(i)} \cos \psi_\alpha^{(i)}, p_{y,\alpha}^{(i)} = p_{T,\alpha}^{(i)} \sin \psi_\alpha^{(i)}, p_{z,\alpha}^{(i)} = m_{T,\alpha}^{(i)} \sinh y_\alpha^{(i)} \quad (3)$$

These components decompose the momentum of each particle into Cartesian coordinates, providing additional features for analysis.

The original and derived features are combined into an enriched feature set for each particle, defined as:

$$h_\alpha^{(i)} = \left\{ p_{T,\alpha}^{(i)}, y_\alpha^{(i)}, \psi_\alpha^{(i)}, m_{T,\alpha}^{(i)}, E_\alpha^{(i)}, p_{x,\alpha}^{(i)}, p_{y,\alpha}^{(i)}, p_{z,\alpha}^{(i)} \right\}, \quad (4)$$

where  $h_\alpha^{(i)}$  represents the feature vector for particle  $i$  in jet  $\alpha$ . We further calculate aggregate kinematic properties for each jet using the individual particle features. The total momentum vector of a jet  $(\vec{p}_\alpha)$  is obtained by summing the momentum components of its constituent particles:

$$\vec{p}_\alpha = \sum_i \vec{p}_\alpha^{(i)}, \quad (5)$$

with the transverse momentum of the jet  $(p_{T,\alpha})$  calculated as:

$$p_{T,\alpha} = \sqrt{\left( \sum_i p_{x,\alpha}^{(i)} \right)^2 + \left( \sum_i p_{y,\alpha}^{(i)} \right)^2}, \quad (6)$$

which measures the momentum of the jet perpendicular to the beam axis. The jet mass  $(m_\alpha)$  and rapidity  $(\eta_\alpha)$  are defined as:

$$m_\alpha = \sqrt{(E_\alpha^2 - |\vec{p}_\alpha|^2)}, \eta_\alpha = \frac{1}{2} \ln \left( \frac{E_\alpha + p_{z,\alpha}}{E_\alpha - p_{z,\alpha}} \right), \quad (7)$$

where  $E_\alpha$  is the sum of the energies of the jet’s constituent particles and  $p_{z,\alpha}$  is the component of the jet’s momentum along the beam axis.

4) *Edge Construction and Attributes*: These features are then normalized by their maximum values across all jets to ensure consistent input scales, enhancing the stability of the training process. Edges between particles in a jet are defined based on the spatial proximity of particles in the  $(\psi, y)$  plane, calculated using the Euclidean distance:

$$\Delta R_\alpha^{(ij)} = a_\alpha^{(ij)} = \sqrt{\left( \psi_\alpha^{(i)} - \psi_\alpha^{(j)} \right)^2 + \left( y_\alpha^{(i)} - y_\alpha^{(j)} \right)^2} \quad (8)$$

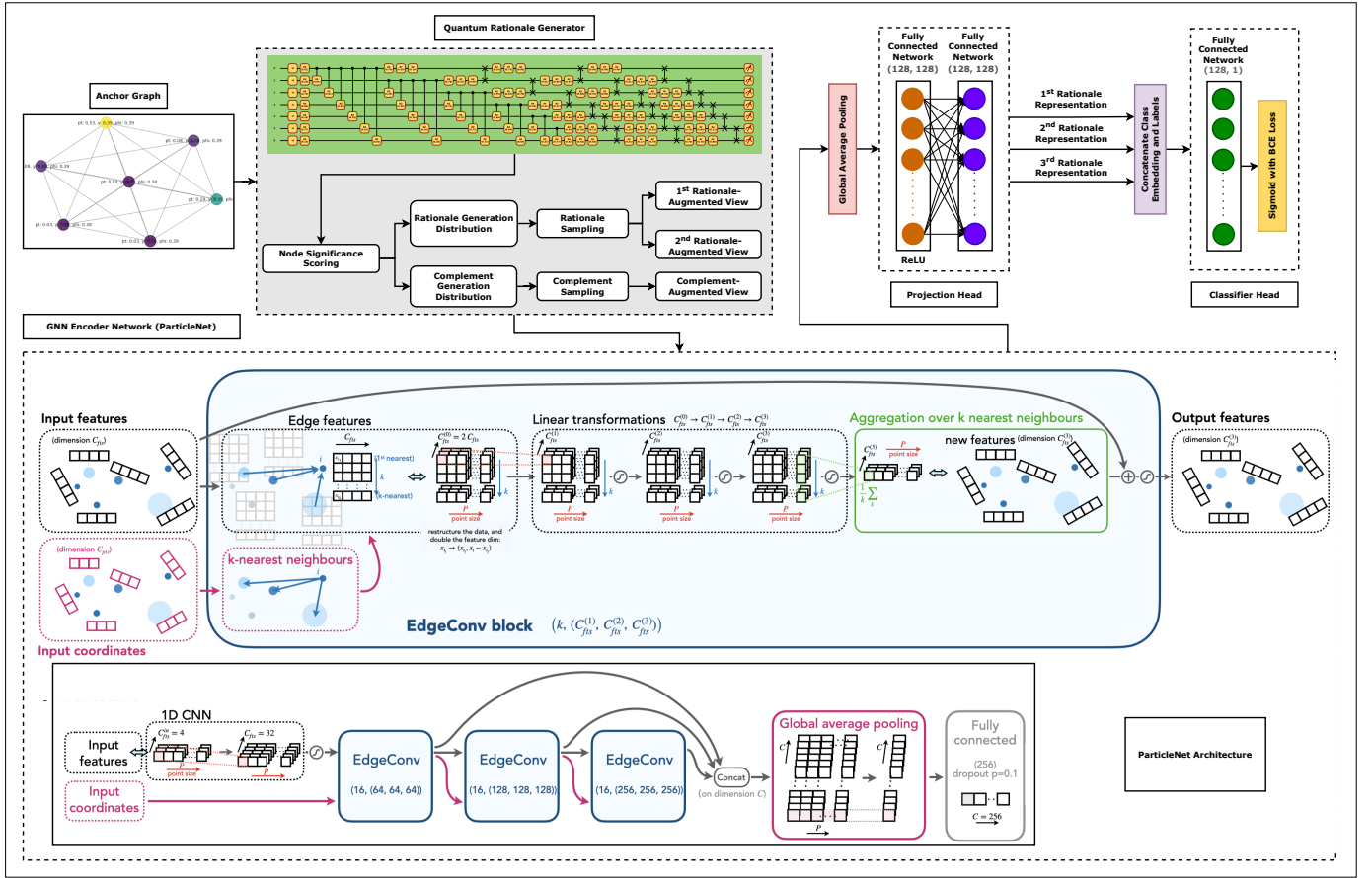


Fig. 1. QRGCL framework. The quantum rationale generator identifies a discriminative subset of nodes in the original graph. The rationale generator shared GNN-encoder, and projection head is jointly optimized by minimizing the combined loss.

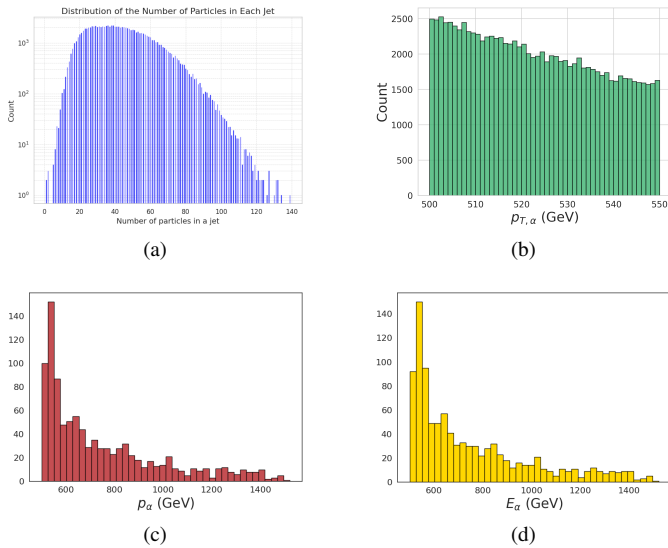


Fig. 2. Distribution of (a) number of particles in each jet, (b) transverse momentum, (c) total momenta, and (d) azimuthal angle.

This metric measures the angular separation between two particles, capturing their spatial relationships within the jet. The resulting edge attribute matrix  $\Delta R_{\alpha}^{(ij)} = a_{\alpha}^{(ij)}$  is used as input for graph-based models to encode the spatial structure

of the jet.

5) *Graph-Based Augmentation and Contrastive Learning:* Next, the preprocessed graph data creates pairs or “views” as input for our CL framework. In CL, pairs of similar and dissimilar views are generated to help the model learn discriminative representations. Positive views are created by taking a graph and generating an augmented version of it, such as applying transformations like node dropping, edge perturbation, or feature masking. For instance, an augmented view of a quark jet remains labeled as similar (1), while a dissimilar pair may consist of a quark jet and a gluon jet, labeled as 0. The differentiation between positive and negative pairs is established solely through the loss function, with the model lacking an inherent understanding of the concept of ‘view’. The loss function guides the model toward clustering similar samples in proximity. Figure 3b shows positive and negative pairs created for our CL process. The distorting jets method was applied to shift the positions of the jet constituents independently, with shifts drawn from a normal distribution. The shift is applied to each constituent’s  $\eta$  and  $\psi$  values, scaled by their  $p_T$ , ensuring that lower  $p_T$  particles experience more significant shifts. The collinear fill technique added collinear splittings to the jets, filling zero-padded entries by splitting existing particles. A random proportion is applied for each selected particle to create two new particles that share the original momentum and position information.

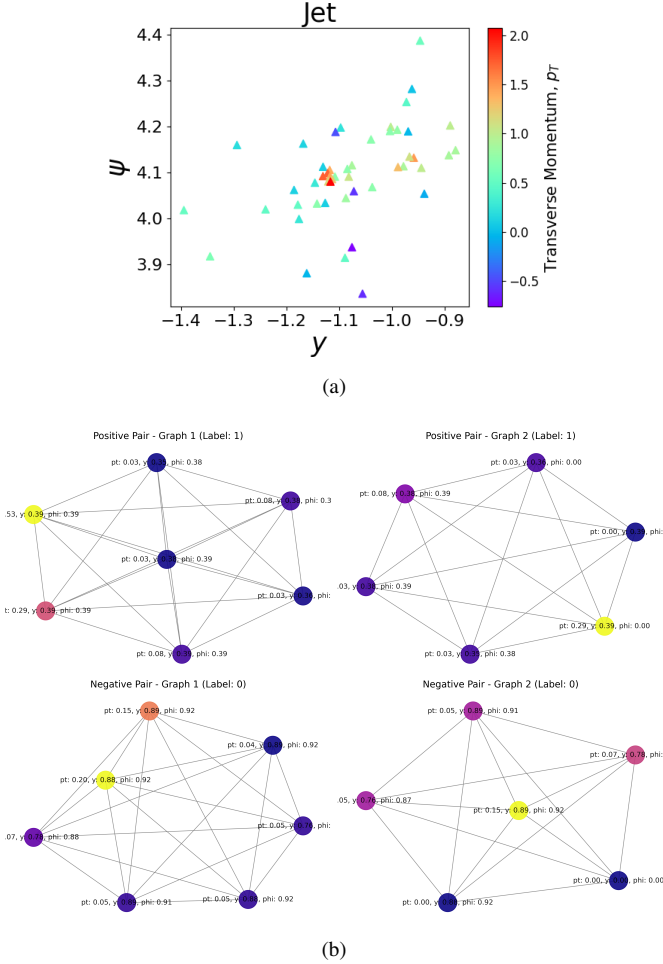


Fig. 3. Plot of (a) a sample jet shown in  $(\psi, y)$  plane with each particle color-coded by its  $p_{T,\alpha}^{(i)}$ , (b) a sample of graph views used in our CL-based approach. Each graph represents a jet as a collection of nodes (particles) with associated physics-based features. The graphs are undirected, reflecting the bidirectional nature of interactions between particles.

6) *Enforcing Infrared and Collinear Safety*: To ensure that our methodology adheres to the principles of infrared and collinear (IRC) safety, we follow the guidelines established by Dillon et al. [14] to avoid sensitivities to soft and collinear emissions, which are irrelevant to the physical properties of jets. Infrared safety is maintained by applying small perturbations to the  $\eta'$  and  $\psi'$  of soft particles. These perturbations follow normal distributions,  $\eta' \sim \mathcal{N}(\eta, \frac{\Lambda_{\text{soft}}}{p_T})$  and  $\psi' \sim \mathcal{N}(\psi, \frac{\Lambda_{\text{soft}}}{p_T})$ , where  $\Lambda_{\text{soft}} = 100 \text{ MeV}$  and  $p_T$  is the transverse momentum of the jet. Collinear safety is ensured by requiring that the sum of the transverse momenta of two collinear particles equals the total transverse momentum of the jet:  $p_{T,\alpha} + p_{T,\beta} = p_T$ . Additionally, the  $\eta$  and  $\psi$  of the two particles are kept identical, i.e.,  $\eta_a = \eta_b = \eta$  and  $\phi_a = \phi_b = \phi$ , preserving the collinear structure of the jet during training and testing. Techniques like node dropping and edge perturbation alter the graph's structure by randomly removing or changing connections between nodes. This helps to train the model with varying graph structures, ensuring it can adapt to different particle distributions and topologies.

7) *Data Splitting*: To ensure manageable computational complexity and adapt the model for quantum processing, we focused on jets containing at least ten particles, resulting in a dataset of  $N = 1,997,445$  jets, of which 997,805 were classified as quark jets. Unlike classical graph neural networks (GNNs), which offer flexibility in adjusting the number of hidden features, quantum networks are constrained by the scaling of quantum states and Hamiltonians. Specifically, the quantum computational cost scales as  $2^n$ , where  $n$  represents the number of qubits, corresponding to the number of nodes ( $n_\alpha$ ) in the graph. Each node represents a particle in the jet, making jets with many particles challenging to handle due to the exponential growth in quantum computational requirements.

To address the challenge of varying particle numbers in jets, we simplified the problem by limiting the number of active nodes (particles) per jet to  $n_\alpha = 7$ . This was done by selecting the seven particles with the highest transverse momentum ( $p_T$ ) from each jet. Consequently, each jet graph is represented by a feature set  $h_\alpha = (h_\alpha^{(1)}, h_\alpha^{(2)}, \dots, h_\alpha^{(7)})$ , where each  $h_\alpha^{(i)} \in \mathbb{R}^8$  corresponds to the enriched feature vector of a particle. The complete representation of each jet is thus given by  $h_\alpha \in \mathbb{R}^{7 \times 8}$ , capturing key physical attributes of the selected particles. A subset of  $N = 12,500$  jets was randomly selected for model training, with 10,000 jets used for training, 1,250 for validation, and 1,250 for testing. These subsets maintained the original class distribution, resulting in 4,982 quark jets in the training set, 658 in the validation, and 583 in the testing set.

### B. Proposed QRGCL

Quantum rationale-aware GCL (QRGCL) consists of 4 major components, as illustrated by Figure 1: rationale generator (RG), encoder network, projection head, and loss function.

1) *Quantum Rationale Generator (QRG)*: The QRGCL model substitutes its classical RG (CRG) with a quantum RG (QRG). This component is crucial in generating augmented graph representations by assigning significance scores to each node. The QRG is built using a 7-qubit parameterized quantum circuit (PQC), where each qubit represents a node in the graph.

The quantum circuit for the QRG consists of 3 main components, as shown in Figure 4: *data encoding*, *parameterized unitaries*, and *entanglement*. The encoding process starts by initializing each qubit, typically using a Hadamard ( $H$ ) gate to create a uniform superposition state:

$$H|0\rangle = \frac{1}{\sqrt{2}}(|0\rangle + |1\rangle). \quad (9)$$

Next, node feature vectors are encoded using rotation gates, with various encoding options such as  $RX$ ,  $RY$ ,  $RZ$ , or  $H$  gates. The specific choice of encoding can be customized, with  $RX$  encoding being implemented for proposed angle-based representations: Node feature vectors  $\mathbf{x}_i$  are encoded as rotation angles using  $RX$ ,  $RY$ , or  $RZ$  gates. For example, the  $RX$  gate is defined as:

$$RX(\theta) = \begin{pmatrix} \cos(\theta/2) & -i \sin(\theta/2) \\ -i \sin(\theta/2) & \cos(\theta/2) \end{pmatrix} \quad (10)$$

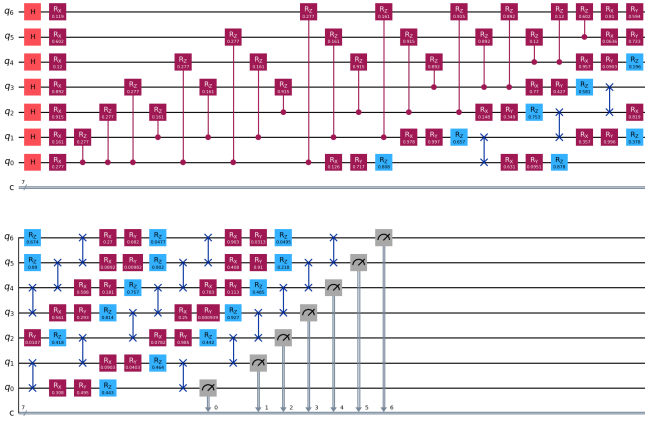


Fig. 4. QRG circuit of the proposed QRGCL. The circuit operates on seven qubits, with each qubit corresponding to a node in the graph. The top portion shows the data encoding stage, where each qubit is initialized using a  $H$  gate followed by  $RX$ -based angle encoding node features.  $CRZ$  gates encode edge relationships between qubits. The bottom portion includes parameterized rotations ( $RX$ ,  $RY$ ,  $RZ$ ) for adaptable representations and entanglement layers using  $SWAP$  gates. Measurement results are obtained on a computational basis, with classical registers collecting the output.

where  $\theta$  is determined by the value of  $x_i$ . Edge relationships are encoded using controlled-phase ( $CRZ$ ) gates between pairs of qubits. This is a diagonal, asymmetric gate that applies a phase to the target qubit depending on the control qubit's state:

$$CRZ(\theta) = \begin{pmatrix} 1 & 0 & 0 & 0 \\ 0 & 1 & 0 & 0 \\ 0 & 0 & 1 & 0 \\ 0 & 0 & 0 & e^{i\theta} \end{pmatrix} \quad (11)$$

After encoding, each qubit undergoes parameterized  $U3$  gates, defined as:

$$U3(\theta, \phi, \lambda) = \begin{pmatrix} \cos(\theta/2) & -e^{i\lambda} \sin(\theta/2) \\ e^{i\phi} \sin(\theta/2) & e^{i(\phi+\lambda)} \cos(\theta/2) \end{pmatrix} \quad (12)$$

which allows the QRG to learn adaptable representations through trainable parameters  $\theta$ ,  $\phi$ , and  $\lambda$ . These parameterized gates form the trainable part of the circuit, allowing the QRG to adaptively learn the significance scores based on the input data during training. The parameters of these gates are optimized through gradient-based approaches. Entanglement is introduced using a flexible choice of entanglement layers, such as  $CNOT$ ,  $CZ$ ,  $SWAP$ , or their butterfly-pattern variants. These entanglement patterns are designed based on the graph's structure and ensure that important correlations between nodes are captured. For example,  $SWAP$  gates can exchange quantum states between qubits, preserving relationships between specific nodes:

$$SWAP = \begin{pmatrix} 1 & 0 & 0 & 0 \\ 0 & 0 & 1 & 0 \\ 0 & 1 & 0 & 0 \\ 0 & 0 & 0 & 1 \end{pmatrix}. \quad (13)$$

The output of the QRG is obtained by measuring the qubits on a computational basis. The squared amplitudes of states

with a Hamming weight of 1 (e.g.,  $|00001\rangle, |00010\rangle, \dots$ ) provide node significance scores normalized into a discrete probability distribution. With the QRG generating significance scores, augmented views are created for the downstream CL process. For an optimistic view, nodes with the highest significance scores are retained, preserving the most relevant information for classification. Negative views, on the other hand, are constructed by using less significant nodes or by introducing random variations, helping the model learn to distinguish between genuinely informative structures and noise.

2) *Encoder Network*: We used the ParticleNet [2] model as our encoder to convert the augmented views of input particle features into low-dimensional embeddings. ParticleNet is a graph-based neural network optimized for jet tagging, leveraging dynamic graph convolutional neural networks (DGCNN) to process unordered sets of particles, treating jets as particle clouds.

The input to the encoder is a matrix  $\mathbf{X} \in \mathbb{R}^{n \times d}$ , where  $n$  represents the number of particles and  $d$  the feature dimension (e.g., momentum, energy). ParticleNet constructs a  $k$ -nearest neighbor ( $k$ -NN) graph, connecting each particle to its  $k$  closest neighbors in feature space. The EdgeConv block begins by computing the  $k$  nearest neighbors using the particles' spatial coordinates. Edge features are constructed based on the feature vectors of these neighbors. The core operation of EdgeConv is a 3-layer multi-layer perceptron (MLP), where each layer consists of a linear transformation, batch normalization, and a ReLU activation. To improve information flow and avoid vanishing gradients, a shortcut connection inspired by general ResNet architecture runs parallel to the EdgeConv operation, allowing input features to bypass the convolution layers. The two main hyperparameters of each EdgeConv block are  $k$ , the number of nearest neighbors, and  $C = (C_1, C_2, C_3)$ , the number of units in each MLP layer.

ParticleNet's architecture consists of three EdgeConv blocks. In the first block, distances between particles are computed in the pseudorapidity-azimuth ( $\eta, \psi$ ) plane. In the following blocks, learned feature vectors from the previous layers serve as the coordinates. The number of nearest neighbors  $k$  is 16 across all blocks. The channel configurations  $C$  are (64, 64, 64), (128, 128, 128), and (256, 256, 256), respectively, indicating the units per MLP layer. After the EdgeConv blocks, global average pooling aggregates the learned features from all particles into a single vector. This vector is passed through a fully connected layer with 256 units and a ReLU activation. A dropout layer with a 0.1 probability is applied to prevent overfitting before the final fully connected layer. The output layer, with two units and a softmax function, produces the jet-level embeddings. These embeddings are then weighted according to node importance scores, emphasizing the most relevant particles. A global mean pooling operation is used further to aggregate the weighted features into a fixed-size jet representation.

3) *Projection Head*: Our architecture incorporates a projection head that effectively maps high-dimensional embeddings from the encoder into compact, CL-optimized latent space. This distinction allows the encoder to learn features suited for downstream tasks while the projection head focuses on maxi-

mizing contrastive effectiveness. This projection head employs an initial linear transformation to reduce the dimensionality of the input embedding (128-dimensional) to a latent space of the same dimensionality, followed by a ReLU activation and a final linear layer. This layered design allows the projection head to align representations tightly with the CL objective by enforcing mutual information between anchor and rationale representations in the latent space.

4) *Quantum-Enhanced Contrastive Loss*: QRGCL model uses a carefully designed loss function that integrates multiple elements—InfoNCE, alignment, uniformity, rationale-aware loss (RA loss), and contrastive pair loss (CP loss)—to optimize the learning of quantum-enhanced embeddings.

**InfoNCE Loss**: The InfoNCE loss focuses on distinguishing positive pairs from negative pairs. It is defined as:

$$\mathcal{L}_{\text{InfoNCE}} = -\log \left( \frac{e^{(\text{sim}(\mathbf{z}_i, \mathbf{z}_2)/T)}}{\sum_{j=1}^N \mathbb{1}_{j \neq i} e^{(\text{sim}(\mathbf{z}_i, \mathbf{z}_j)/T)}} \right) \quad (14)$$

where  $\mathbf{z}_i$  and  $\mathbf{z}_2$  are embeddings of a positive pair,  $T$  is the temperature parameter, and  $N$  is the batch size. The temperature parameter helps control the sharpness of the similarity scores, making the model more or less sensitive to differences between pairs.

**RA Loss**: The RA loss is designed to focus on the “rationale” of the graph—subsets of nodes that contain critical classification information. This is calculated as:

$$\mathcal{L}_{\text{RA}} = -\log \left( \frac{e^{(\text{sim}(\mathbf{z}_1, \mathbf{z}_2)/T)}}{\sum_{j=1}^N e^{(\text{sim}(\mathbf{z}_1, \mathbf{z}_j)/T)} - e^{(\text{sim}(\mathbf{z}_1, \mathbf{z}_2)/T)}} \right) \quad (15)$$

The RA loss ensures that the model concentrates on similarities between positive pairs while minimizing the influence of other relationships.

**CP Loss**: The CP loss encourages the model to distinguish between positive pairs and a complement set (pairs involving nodes not deemed crucial for the classification task):

$$\mathcal{L}_{\text{CP}} = -\log \left( \frac{e^{(\text{sim}(\mathbf{z}_1, \mathbf{z}_2)/T)}}{\sum_{j=1}^N e^{(\text{sim}(\mathbf{z}_1, \mathbf{z}_3)/T)} + e^{(\text{sim}(\mathbf{z}_1, \mathbf{z}_2)/T)}} \right) \quad (16)$$

where  $\mathbf{z}_3$  represents embeddings from the complement set. This loss helps the model differentiate genuine relationships between similar samples from spurious correlations by learning from pairs with varying significance.

**Alignment Loss**: It measures the closeness of normalized embeddings of positive pairs ( $p_{\text{pos}}$ ):

$$\mathcal{L}_{\text{align}} \triangleq \mathbb{E}_{(x,y) \sim p_{\text{pos}}} [\|\text{normalize}(\mathbf{z}_1) - \text{normalize}(\mathbf{z}_2)\|^2] \quad (17)$$

We used *quantum state fidelity* as a distance metric, replacing the traditional  $L^2$  distance typically used in classical CL. Quantum fidelity measures the closeness between two quantum states. Thus, alignment loss becomes:

$$\mathcal{L}_{\text{align}} \triangleq \mathbb{E}_{(x,y) \sim p_{\text{pos}}} [1 - \mathcal{F}(\mathbf{z}_1, \mathbf{z}_2)] = 1 - \left( \text{Tr} \left( \sqrt{\sqrt{\mathbf{z}_1} \mathbf{z}_2 \sqrt{\mathbf{z}_1}} \right) \right)^2 \quad (18)$$

where  $\rho_1$  and  $\rho_2$  are density matrices of the quantum states. This metric replaces the usual Euclidean distance in the alignment term of the loss function.

**Uniformity Loss**: It ensures that embeddings are uniformly

distributed over the hypersphere, avoiding representation collapse:

$$\mathcal{L}_{\text{uniform}} \triangleq \log \mathbb{E}_{(x,y) \sim p_{\text{data}}} \left[ e^{(-2 \text{pdist}(\mathbf{z}))} \right] \quad (19)$$

where  $\text{pdist}$  calculates the pairwise distances between embeddings. This helps maintain representation diversity, allowing the model to capture more nuanced differences.

The overall loss for the QRGCL model is a weighted combination of the InfoNCE, RA, and CP loss, with optional contributions from the alignment and uniformity terms:

$$\mathcal{L}_{\text{QRGCL}} = \mathcal{L}_{\text{RA}} + \lambda \mathcal{L}_{\text{CP}} + \alpha \mathcal{L}_{\text{align}} + \beta \mathcal{L}_{\text{uniform}} + \delta \mathcal{L}_{\text{InfoNCE}} \quad (20)$$

where  $\lambda$ ,  $\alpha$ ,  $\beta$ , and  $\delta$  are hyperparameters that control the contributions of each loss component. During experimentation, the uniformity term hindered learning, so it can be omitted when necessary.

5) *Classifier Head*: The classifier head follows our GCL framework and consists of a simple neural network with a 128-neuron single linear layer and is designed to perform binary jet discrimination, mapping features to a single output with a sigmoid activation for probabilistic classification.

### C. Benchmarked Models

We developed two classical models (GNN and EQGNN), three quantum models (QGNN, EQGNN, and QCL), five hybrid classical-quantum models (CQCL, 3 QCGCL variants, and QRGCL with  $RX + H$  encoding) (see Table III), and classical counterpart of QRGCL, i.e., CRGCL (see Table II).

1) *Classical RGCL (CRGCL)*: The classical RG (CRG) of RGCL is a GNN estimator designed to generate node representations from graph-structured data, which acts as the counterpart of QRGCL. It consists of three graph convolutional layers (GCN) that reduce feature dimensionality from the input to 32, 16, and finally, 8. Each layer is followed by batch normalization to stabilize training and reduce internal covariate shifts. ReLU activation is applied after the first two layers, while dropout is used to mitigate overfitting. The final output passes through a linear layer to yield a single value per node, followed by softmax for probabilistic representation. For a fair comparison between the CRG and QRG, we use the well-established ParticleNet as the encoder network, followed by the same projection head used in QRGCL.

2) *GNN*: The architecture consists of layers where the message-passing mechanism updates node features based on neighboring nodes and their relationships. An MLP processes the node features in each layer, while an edge MLP aggregates the edge attributes. After several layers, the updated node features are pooled to form a graph-level representation, passing through a fully connected neural network for classification. GNNs can inherently handle the permutation of nodes due to their graph-based nature.

3) *Equivariant GNN (EGNN)*: EGNNs extend GNNs by incorporating symmetry transformations, such as rotational and translational equivariance. This means that the model’s predictions remain consistent under transformations of the input data. The coordinates of the nodes are updated during each layer based on interactions with neighboring nodes. The model

utilizes additional features like distance metrics between node pairs to enforce equivariance in graph processing.

4) *Quantum GNN (QGNN)*: In QGNN, the graph’s node features are embedded into quantum states using an embedding layer. These quantum states evolve under a parameterized Hamiltonian, which encodes the interactions between nodes (qubits) based on the graph’s adjacency matrix. The QGNN model relies on unitary transformations to evolve the quantum state over multiple layers. After the final layer, quantum measurements are performed, and the results are passed through a fully connected layer to make predictions.

5) *Equivariant Quantum GNN (EQGNN)*: EQGNNs [15] are quantum analogs of EGNNs, incorporating equivariance into the quantum architecture. Like QGNNs, EQGNNs operate on quantum states but ensure that the learned representations are equivariant under symmetries, such as permutations or rotations. The final quantum states are aggregated through pooling, ensuring the network remains permutation-equivariant. This aggregation is followed by classical post-processing to yield the model’s predictions.

6) *QCL*: QCL employs a quantum convolutional neural network (QCNN) with input size  $18 \times 18$  with zero padding as the encoder, where data-reuploading circuits (DRCs) replace classical convolutional kernels. The QCNN consists of 2 similar layers: the first with a  $(3 \times 3)$  kernel, stride 2, and 3-qubit DRC as filter. The final encoding size after flattening is 16. The projection network either uses a 2-node linear layer.

7) *Classical-Quantum CL (CQCL)*: Hybrid CQCL is similar to QCL except for the final projection head, which uses a  $\log_2^{d=2}$  qubit ( $d = \text{embedding dimension}$ ) DRC circuit. To evaluate the ability of QCL and CQCL to generate generalized representations, we make predictions using a simple MLP, an input layer of size 256, and a hidden layer of size 32, both with BatchNorm and LeakyReLU.

8) *Quantum-Classical GCL (QCGCL)*: QCGCL architecture initially uses multiple layers of graph attention-based convolution (GATConv) layers to capture graph features. Each GAT layer is followed by batch normalization and residual connections, which allow the model to skip layers for improved training. The graph-level embedding is achieved through mean and max pooling. A quantum circuit then processes this pooled GNN output. We benchmarked QCGCL using 3 different quantum encoders, as depicted in Table III. Finally, the GNN and quantum outputs are concatenated and passed through a fully connected readout layer to generate the final prediction.

## IV. EXPERIMENTAL SETUP

### A. Simulation Tools and Environment

We implemented all the models using the *PyTorch* framework for classical computations and *Pennylane* for quantum circuit simulation. We used the *Deep Graph Library (DGL)* to handle graph operations and the *Qiskit* framework to simulate quantum circuits. The computing infrastructure consisted of Intel(R) Xeon(R) CPUs (x86) with a clock frequency of 2 GHz, equipped with 4 vCPU cores and 30 GB of DDR4 RAM. For GPU acceleration, we leveraged two NVIDIA T4

TABLE I  
HYPERPARAMETER OPTIMIZATION RESULTS OF THE PROPOSED QRGCL

Parameter type	Parameter	Test Accuracy	AUC	F1 Score
Encoder type	Amplitude	69.30%	74.69%	69.30%
	IQP	68.90%	76.10%	68.47%
	Displacement-amplitude	66.17%	72.10%	65.97%
	Displacement-phase	70.17%	76.22%	69.13%
	RY	67.00%	73.93%	67.00%
	<b>RX</b>	<b>70.80%</b>	<b>76.30%</b>	<b>69.60%</b>
	RZ	62.90%	67.32%	62.80%
	<b>H</b>	<b>70.83%</b>	<b>76.71%</b>	<b>69.65%</b>
Learning rate	Phase	68.50%	74.21%	68.30%
	<b>1E-03</b>	<b>70.30%</b>	<b>76.20%</b>	<b>70.29%</b>
	1E-04	68.60%	74.41%	68.39%
	1E-02	69.50%	75.81%	69.47%
	3E-03	63.90%	68.83%	63.70%
	5E-03	66.00%	70.89%	65.99%
Entanglement type	CNOT	69.80%	76.58%	69.79%
	CZ	68.20%	73.45%	68.14%
	<b>SWAP</b>	<b>71.00%</b>	<b>76.20%</b>	<b>70.79%</b>
	CNOT Butterfly	68.00%	74.63%	67.98%
	CZ Butterfly	67.70%	73.20%	67.69%
	SWAP Butterfly	68.00%	73.21%	67.79%

GPUs, each with 2560 CUDA cores and 16 GB of VRAM, significantly boosting the performance of deep learning tasks.

### B. Hyperparameters and Configurations

We varied the hyperparameters related to CRG, QRG, data augmentation, and training for the proposed QRGCL model, highlighting the test accuracy, AUC, and F1 scores across various encoder types, learning rates (LR), and entanglement strategies. We used Adam optimizer with a  $1 \times 10^{-3}$  learning rate across all the models and a binary cross-entropy loss function. 10-fold cross-validation was performed for each model, and the mean and standard deviation were calculated for each metric. The hidden feature size for classical GNN and EGNN was 10, while for the QGNN and EQGNN, it was  $2^{n_\alpha} = 8$ . In the case of QCL and CQCL,  $n_{layer}$  stands for the depth of the quantum circuit, and in other models, it refers to the number of GNN layers.

The choice of epochs and batch sizes varies based on the computational requirements of classical and quantum models. Classical models like GNN and EGNN use larger batch sizes (64) and fewer epochs (19) to leverage efficient gradient updates, allowing faster convergence. In contrast, quantum models such as QGNN and EQGNN use much smaller batch sizes (1) due to quantum hardware limitations yet still require 19 epochs to ensure adequate learning despite more minor updates per step. For fully quantum and hybrid models like QRGCL and QCGCL, larger batch sizes (2000) and more epochs (50) are used due to the longer backpropagation caused by the complex custom loss function, with multiple loss components ensuring that the model has sufficient time to learn robust quantum-based representations, as the slower convergence can hinder effective learning.

## V. RESULTS AND DISCUSSION

We evaluated the performance of QRGCL against two classical models (GNN and EQGNN), three quantum models (QGNN, EQGNN, and QCL), and five hybrid classical-quantum models (CQCL, three variants of QCGCL, and QRGCL with RX+H encoding). The area under the curve (AUC) was selected as the benchmark metric due to its

TABLE II  
COMPARISON BETWEEN CLASSICAL AND QUANTUM RG OF RGCL.

Parameter type	Parameter	Classical RG			Quantum RG		
		Test Accuracy	AUC	F1-score	Test Accuracy	AUC	F1-score
Nodes per graph	7	70.40%	<b>76.31%</b>	69.13%	70.80%	<b>75.91%</b>	69.86%
	8	68.20%	74.09%	67.90%	70.80%	75.61%	70.50%
	9	68.40%	73.38%	67.15%	67.60%	74.46%	67.54%
	10	67.00%	73.37%	66.50%	70.70%	75.74%	70.30%
Number of layers	2	68.80%	74.51%	68.80%	66.80%	71.42%	66.49%
	3	66.70%	73.58%	66.70%	68.60%	<b>74.71%</b>	68.50%
	4	71.20%	<b>76.29%</b>	71.08%	66.40%	72.34%	66.39%
	5	63.00%	67.45%	62.99%	67.40%	71.16%	67.28%
Augmentation ratio	<b>0.1</b>	67.80%	<b>74.09%</b>	67.78%	72.10%	<b>78.78%</b>	72.10%
	0.2	64.60%	69.78%	64.49%	65.60%	71.14%	65.59%
	0.3	63.70%	69.57%	63.70%	71.30%	76.95%	71.28%

TABLE III  
PERFORMANCE BENCHMARKING AND ABLATION TEST OF THE PROPOSED QRGCL. **BOLD** INDICATES THE BEST PERFORMANCE.

Model	Test accuracy	AUC	F1 score	# Parameters	$n_\alpha$	$n_{layer}$	Batch size	Epoch	Encoder
QGNN	72.20%±2.62%	70.37%±2.09%	72.09%±2.44%	5156	3	6	1	19	MLP + H
GNN	73.90%±1.78%	63.36%±0.89%	73.93%±1.34%	5122	3	5	64	19	MLP
EGNN	73.90%±0.89%	67.88%±0.45%	73.55%±0.89%	5252	3	4	64	19	MLP
EQGNN	71.40%±2.23%	74.36%±1.78%	71.22%±1.45%	5140	3	6	1	19	MLP + H
QCL	50.40%±1.29%	53.26%±0.48%	51.49%±0.68%	280	3	3	256	1000	Amplitude
CQCL	50.00%±0.75%	49.79%±1.50%	48.33%±1.29%	250	3	3	256	1000	Amplitude
QCGCL	57.44%±1.46%	62.26%±1.56%	56.72%±1.56%	7448	7	6	128	50	Angle (RY+RX)
QCGCL	65.39%±1.02%	71.07%±0.48%	63.80%±1.02%	7448	7	6	128	50	Angle (RY)
QCGCL	65.33%±1.26%	70.83%±0.78%	64.52%±1.53%	7448	7	6	128	50	Amplitude + Angle (RY)
QRGCL variant	70.93%±0.99%	77.30%±1.77%	70.40%±1.67%	126015	7	3	2000	50	RX + H
<b>Proposed QRGCL</b>	71.50%±0.82%	<b>77.53%±0.88%</b>	70.35%±0.82%	126015	7	3	2000	50	<b>H + RX</b>

effectiveness in assessing binary classification performance across all thresholds. The number of trainable parameters of CRG was 1,073, compared to 45 for QRG.

The hyperparameters specific to QRGCL include encoder type, learning rate, and entanglement type, as detailed in Table I. Among the encoders, *RX* and Hadamard (*H*) achieved the highest AUC values at 76.30% and 76.71%, respectively, while displacement-amplitude and *RZ* encodings performed poorly, with AUCs of 72.10% and 67.32%. The optimal learning rate of  $1 \times 10^{-3}$  produced the highest AUC of 76.20%, with higher rates resulting in decreased performance. The *SWAP* entanglement type yielded the best overall results, achieving an AUC of 76.20%. *CNOT* and *CZ* entanglements performed strongly, while other configurations underperformed. For the proposed QRGCL, two possible combinations of *RX* and *H* encoders the learning rate of  $1 \times 10^{-3}$  and *SWAP* entangler were tried.

For both the classical RGCL and QRGCL models, tunable parameters included the number of nodes per head ( $n_\alpha$ ) ranging from 7 to 10, the number of classical or quantum layers ( $n_{layer}$ ) ranging from 2 to 5, and the augmentation ratio ranging from 0.1 to 0.3. As shown in Table II, QRGCL outperforms the classical RGCL with 8 and 10 nodes, achieving higher AUC values. At 3 layers, QRGCL surpasses the classical model, achieving 74.71% compared to 73.58%. However, it underperformed at 2 and 4 layers. With a 0.1 augmentation ratio, QRGCL significantly outperformed the classical approach, achieving 78.78% compared to 74.09%. Overall, the optimal parameters for QRGCL were found to be

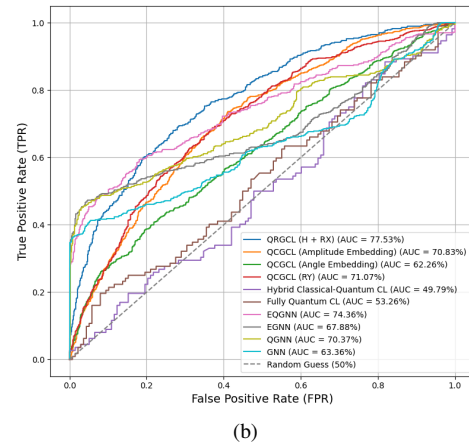
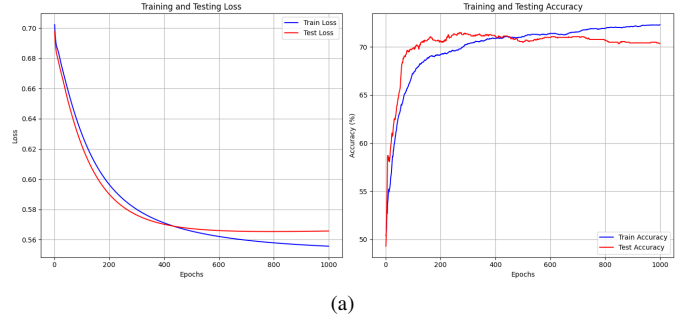


Fig. 5. (a) Training and testing dynamics of QRGCL over 1000 epochs. The left graph illustrates loss curves, while the right graph presents accuracy curves. (b) ROC-AUC curve for all the benchmarked models

$n_\alpha = 7$ ,  $n_{layer} = 3$ , and an augmentation ratio of 10%.

Based on Table III and Figure 5b, it is evident that our proposed QRGCL model achieves the highest AUC score (77.53%). We took the best two well-performing encoders from Table I and developed two variants hybridizing them, and further experimentations revealed that  $H$  followed by  $RX$  gate is more robust. Additionally, the relatively large number of parameters in the QRGCL is due to the utilization of the ParticleNet GNN encoder, which possesses 125k parameters, while the QRG circuit only has 45 parameters. Tables I, II, and III complement the ablation studies for QRGCL by presenting results for configurations without rationale-awareness (QGNN, GNN, EGNN, EQGNN), analyzing VQC components (such as encoding variants, entanglement structures, and variations in qubits and layers), exploring different classical-quantum interfaces (including quantum-only and hybrid architectures, as well as a classical-only baseline), and examining the effects of rationale-guided data augmentation. Figure 5a shows both training and testing losses decrease steadily in QRGCL, indicating practical training with a continuous reduction in error. By around 800 epochs, the losses stabilize, suggesting that the model has reached a convergence point where further training yields minimal improvements. The small gap between the two loss curves suggests minimal overfitting and generalization of test data. Both training and testing accuracies rise sharply within the first 200 epochs, reflecting rapid learning and an effective initial adjustment of model parameters. Around 800 epochs, both accuracies stabilize. The test accuracy levels off slightly above 70%, while training accuracy remains close but slightly lower. This stability indicates that QRGCL has reached its maximum performance capacity on this dataset, with limited fluctuations.

## VI. CONCLUSION

This paper introduced QRGCL, a hybrid quantum-classical rationale-aware GNN for quark-gluon jet classification, integrating quantum computation with GCL. Our results show that QRGCL outperforms two classical, three quantum, and five hybrid classical-quantum models, achieving an AUC of 77.53%. Hyperparameter tuning indicated that  $H + RX$  encoder and  $SWAP$  entanglement gate optimized performance, emphasizing the importance of careful circuit design in quantum models. QRGCL performed best on smaller graphs (7 nodes) with low augmentation (0.1), achieving an AUC of 78.78%, indicating their value for compact, high-quality representations. Ablation studies showed that the QRG benefits from a 3-layer architecture, while the CRG performs best with four layers, underscoring the potential of quantum-enhanced approaches in particle physics. Future work could focus on reducing parameter complexity to streamline model efficiency, try other state-of-the-art encoder networks like LorentzNet, and also the hybridization of RG. We also plan to extend the model to other high-energy physics tasks, such as anomaly detection in particle collisions and event reconstruction. We look forward to improving the explainability of GCL and exploring how retrospective and introspective learning in rationale discovery can guide discrimination tasks and enhance the generalization of backbone models.

## REFERENCES

- [1] R. Kogler, B. Nachman, A. Schmidt, L. Asquith, E. Winkels, M. Campanelli, C. Delitzsch, P. Harris, A. Hinzmann, D. Kar, C. McLean, J. Pilot, Y. Takahashi, N. Tran, C. Vernieri, and M. Vos, "Jet substructure at the Large Hadron Collider," *Reviews of Modern Physics*, vol. 91, no. 4, p. 045003, Dec. 2019, publisher: American Physical Society. [Online]. Available: <https://link.aps.org/doi/10.1103/RevModPhys.91.045003>
- [2] H. Qu and L. Gouskos, "Jet tagging via particle clouds," *Physical Review D*, vol. 101, no. 5, p. 056019, Mar. 2020, publisher: American Physical Society. [Online]. Available: <https://link.aps.org/doi/10.1103/PhysRevD.101.056019>
- [3] S. Li, X. Wang, A. Zhang, Y. Wu, X. He, and T.-S. Chua, "Let invariant rationale discovery inspire graph contrastive learning," in *Proceedings of the 39th International Conference on Machine Learning*, ser. Proceedings of Machine Learning Research, K. Chaudhuri, S. Jegelka, L. Song, C. Szepesvari, G. Niu, and S. Sabato, Eds., vol. 162. PMLR, 17–23 Jul 2022, pp. 13 052–13 065. [Online]. Available: <https://proceedings.mlr.press/v162/li22v.html>
- [4] P. Veličković, "Everything is connected: Graph neural networks," *Current Opinion in Structural Biology*, vol. 79, p. 102538, Apr. 2023. [Online]. Available: <https://www.sciencedirect.com/science/article/pii/S0959440X2300012X>
- [5] Y. You, T. Chen, Y. Sui, T. Chen, Z. Wang, and Y. Shen, "Graph contrastive learning with augmentations," in *Proceedings of the 34th International Conference on Neural Information Processing Systems*, ser. NIPS '20. Red Hook, NY, USA: Curran Associates Inc., Dec. 2020, pp. 5812–5823.
- [6] M. Larocca, N. Ju, D. García-Martín, P. J. Coles, and M. Cerezo, "Theory of overparametrization in quantum neural networks," *Nature Computational Science*, vol. 3, no. 6, pp. 542–551, June 2023, publisher: Nature Publishing Group. [Online]. Available: <https://www.nature.com/articles/s43588-023-00467-6>
- [7] N. Yoshioka, T. Okubo, Y. Suzuki, Y. Koizumi, and W. Mizukami, "Hunting for quantum-classical crossover in condensed matter problems," *npj Quantum Information*, vol. 10, no. 1, pp. 1–10, Apr. 2024, publisher: Nature Publishing Group. [Online]. Available: <https://www.nature.com/articles/s41534-024-00839-4>
- [8] Y. Mo, X. Wang, S. Fan, and C. Shi, "Graph Contrastive Invariant Learning from the Causal Perspective," *Proceedings of the AAAI Conference on Artificial Intelligence*, vol. 38, no. 8, pp. 8904–8912, Mar. 2024, number: 8. [Online]. Available: <https://ojs.aaai.org/index.php/AAAI/article/view/28738>
- [9] A. Kottahachchi Kankanamge Don, I. Khalil, and M. Atiquzzaman, "A Fusion of Supervised Contrastive Learning and Variational Quantum Classifiers," *IEEE Transactions on Consumer Electronics*, vol. 70, no. 1, pp. 770–779, Feb. 2024, conference Name: IEEE Transactions on Consumer Electronics.
- [10] A. K. K. Don and I. Khalil, "Q-SupCon: Quantum-Enhanced Supervised Contrastive Learning Architecture within the Representation Learning Framework," *ACM Transactions on Quantum Computing*, Apr. 2024, just Accepted. [Online]. Available: <https://dl.acm.org/doi/10.1145/3660647>
- [11] A. Padha and A. Sahoo, "QCLR: Quantum-LSTM contrastive learning framework for continuous mental health monitoring," *Expert Systems with Applications*, vol. 238, p. 121921, Mar. 2024.
- [12] B. Jaderberg, L. W. Anderson, W. Xie, S. Albanie, M. Kiffner, and D. Jaksch, "Quantum self-supervised learning," *Quantum Science and Technology*, vol. 7, no. 3, p. 035005, May 2022, publisher: IOP Publishing. [Online]. Available: <https://dx.doi.org/10.1088/2058-9565/ac6825>
- [13] P. T. Komiske, E. M. Metodiev, and J. Thaler, "Energy flow networks: deep sets for particle jets," *Journal of High Energy Physics*, vol. 2019, no. 1, p. 121, Jan. 2019. [Online]. Available: [https://doi.org/10.1007/JHEP01\(2019\)121](https://doi.org/10.1007/JHEP01(2019)121)
- [14] B. M. Dillon, G. Kasieczka, H. Olschlager, T. Plehn, P. Sorrenson, and L. Vogel, "Symmetries, safety, and self-supervision," *SciPost Physics*, vol. 12, no. 6, p. 188, June 2022. [Online]. Available: [https://www.scipost.org/10.21468/SciPostPhys.12.6.188?acad\\_field\\_slug=all](https://www.scipost.org/10.21468/SciPostPhys.12.6.188?acad_field_slug=all)
- [15] R. T. Forestano, M. Comajoan Cara, G. R. Dahale, Z. Dong, S. Gleyzer, D. Justice, K. Kong, T. Magorsch, K. T. Matchev, K. Matcheva, and E. B. Unlu, "A Comparison between Invariant and Equivariant Classical and Quantum Graph Neural Networks," *Axioms*, vol. 13, no. 3, p. 160, Mar. 2024, number: 3 Publisher: Multidisciplinary Digital Publishing Institute. [Online]. Available: <https://www.mdpi.com/2075-1680/13/3/160>